Local scale wave forecasting aiding harbor safety; A case study in Heraklion Port

Vassiliki Metheniti [0000-0003-2154-5563], Antonios Parasyris [0000-0001-9498-7245], George Alexandrakis [0000-0003-3690-3159], Georgios V. Kozyrakis [0000-0002-5896-6102], Nikolaos A. Kampanis [0000-0001-6231-7730]

Coastal & Marine Research Laboratory (CMRL), Institute of Applied and Computational Mathematics (IACM), Foundation for Research and Technology-Hellas (FORTH), Nik. Plastira 100, Iraklio 700 13, Heraklion, Greece
antonisparasyris@iacm.forth.gr

Abstract. With climate change intensifying wave hazards and storm surges, reliable wave forecasting is essential for harbor safety. This study presents a high-resolution SWAN wave model, specifically tailored for the Port of Heraklion, Greece's third busiest passenger port, to enhance maritime safety and optimize ship scheduling (for entry, departure, and cargo handling) to support environmentally sustainable port operations. The model, dynamically downscaled to 50 m, is under a daily operational run cycle within a packaged application, and provides detailed forecasts of wave heights, crucial for planning cargo operations, optimizing ship disembarkation during adverse weather conditions, and ensuring safer navigation.

Keywords: SWAN model, high-resolution wave models, port safety, port infrastructure, port operations, wave discharge

1 Introduction

The intensification of extreme weather events due to climate change has heightened the risks associated with wave hazards and storm surges, particularly in coastal and port environments. Ports play a critical role in global trade and transportation, yet they are increasingly vulnerable to the impacts of adverse weather conditions, including heightened wave activity and storm surge (Becker et al., 2013; Breivik et al., 2015; Hong, 2013; Sierra et al., 2015; Vousdoukas et al., 2018). These challenges necessitate reliable, high-resolution wave forecasting systems to enhance maritime safety, optimize operational efficiency, and minimize environmental impacts.

The Port of Heraklion, located in Crete, Greece, is the third busiest passenger port in the country and serves as a vital hub for both commercial and passenger maritime traffic (Chatzinikolaou & Arvanitidis, 2016). Ports exposed to open sea conditions and experiencing high volumes of passenger and cargo traffic are particularly susceptible to wave hazards, which can disrupt ship scheduling, delay cargo handling, and compromise safety (Chlomoudis et al., 2024; Papadopoulos & Dermentzopoulos, 1998). To

mitigate the impacts of wave hazards on port operations, an advanced forecasting system capable of providing accurate, localized predictions to support real-time decision-making is proposed in this study.

Implementing an advanced wave forecasting system can significantly benefit various stakeholders by providing accurate, localized predictions that support real-time decision-making. Port authorities can utilize such systems to optimize ship scheduling, minimize delays, and enhance overall operational resilience. For instance, the AccuWaves Operational Forecast Platform offers high-resolution wave forecasts to support safer navigation and efficient port operations (Makris et al., 2024).

Accurate wave forecasts are essential for various maritime activities. Shipping and fisheries depend on precise marine weather forecasts to ensure safety and operational efficiency. Recreational and competitive marine activities, such as boat and yacht racing, as well as swimming events, also benefit from detailed wave condition forecasts, enhancing participant safety and event management. The European Centre for Medium-Range Weather Forecasts (ECMWF) has developed advanced wave forecasting systems to support these applications. For instance, Bidlot (2012) discusses the present status of wave forecasting at ECMWF, highlighting the importance of accurate predictions for maritime operations. Additionally, Breivik et al. (2013) explore wave extremes in the North East Atlantic using ECMWF ensemble forecasts, emphasizing the role of these forecasts in understanding and predicting extreme wave conditions.

Furthermore, the tourism industry, deeply intertwined with maritime activities, gains from improved forecasting capabilities. Accurate wave forecasts contribute to the safety of marine excursions and provide real-time wave condition updates for tourist information systems, fostering a secure and enjoyable experience for visitors engaging with the marine environment. The Wave4Us (wave4us.web.auth.gr) operational platform, for example, offers high-resolution forecasting services beneficial to tourism activities in coastal areas.

This study introduces a high-resolution wave forecasting model tailored specifically for the Port of Heraklion. Based on the SWAN (Simulating WAves Nearshore) model, this system is dynamically downscaled to a resolution of 50 meters, providing detailed insights into wave dynamics within the port area. By leveraging daily operational runs and packaging the application for efficient deployment, the model delivers actionable forecasts to enhance maritime safety and optimize port operations.

The primary objectives of this study are threefold. First, it seeks to demonstrate the feasibility of implementing a high-resolution wave model in a complex operational environment. Second, it aims to illustrate how such forecasts can support environmentally sustainable port operations by reducing unnecessary delays, improving ship scheduling, and ensuring safer navigation. Finally, this study provides a foundation for future applications of high-resolution wave modeling in other coastal regions, addressing both scientific and practical considerations.

2 Methodology

2.1 SWAN model

The SWAN (Simulating WAves Nearshore) model(Booij et al., 1999) is used for the generation of a wave parameters' forecasting system in the region of the Heraklion Port (Fig. 1). SWAN is a third-generation wave model, designed to obtain near-realistic estimates of wind-generated surface gravity waves, especially for shallow regions and it is based on the wave action balance equation with sources and sinks. The directional wave energy density spectrum function is discretized between 0.04 Hz and 0.4 Hz using 36 directional and 24 frequency bins. SWAN runs in third-generation mode for wind input, quadruplet interactions and whitecapping, following a linear wave growth by wind (Cavaleri & Rizzoli, 1981).

For the implementation of a high-resolution forecast, the nesting capability of SWAN is employed. First the wave parameters are computed on a coarse grid corresponding to a larger domain at 24.95° E-25.315° E and 35.32° N-35.565° N (Fig. 1a) at approximately 500 m horizontal grid resolution, and then on a nested finer grid of approximately 50 m resolution (hereinafter SWAN50) at 25.122° E-25.172° E and 35.335° N-35.3645° N (Fig. 1b), producing hourly wave parameters, on a 2-day forecasting horizon. Hourly boundary conditions on the coarse grid, derived from CMEMS (product ID: MEDSEA_ANALYSISFORECAST_WAV_006_017; Korres et al. 2023) at a horizontal resolution of 4.2 km, include sea surface Significant Wave Height (SWH), wave period at maximum variance spectral density, and wave direction at the spectral variance peak. Hourly 10-meter wind velocity components from a dynamically downscaled WRF model, with a 3 km spatial resolution, are used as wind input forcing (Parasyris et al., 2024). The fine grid computation utilizes boundary conditions generated from the coarse grid computation. The bathymetry used for the computation of the coarse grid is derived from EMODNET (*DTM 2022*), with original resolution is 115 * 115 m, and regridded to match the resolution of the coarse model (500 m). For the nested grid the bathymetry is created by the Coastal and Marine Research Laboratory (https://crl.iacm.forth.gr/ last accessed 04/2025) from field measurements, to resolve the coastal topographic features with greater accuracy.

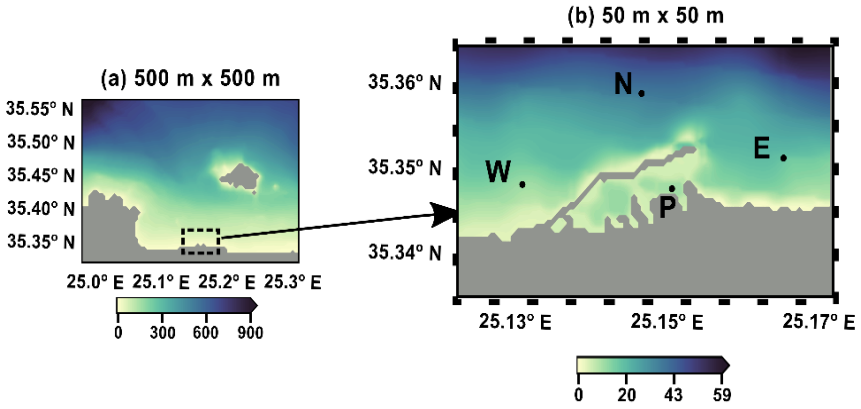

Fig. 1. Bathymetry maps (in m) (a) for the coarse domain (500 m x 500 m horizontal resolution), and (b) for the nested (fine) domain (50 m x 50 m horizontal resolution). In the fine domain the points correspond to the center of 4x4 grid boxes, used for validation and analysis, with annotations for the western, northern, eastern and port points as W (SWAN-W), N (SWAN-N), E (SWAN-E), and P (SWAN-P) respectively

2.2 Application Packaging

In complex modeling systems with multiple nestings and diverse input configurations, end-users must be able to reproduce, test and validate entire workflows on different what-if scenarios and geographical regions. This capability should extend seamlessly across different environments, including local machines, high-performance computing (HPC) clusters, and cloud platforms. Additionally, users should have the flexibility to execute discrete components of the workflow in a modular fashion and integrate them into other workflows as needed. This can be achieved through application packaging, which consists of two primary components.

First, the command-line tools (e.g., Python scripts, shell scripts, C++ programs) and their dependencies are encapsulated within containers and hosted in a container registry, such as Docker Hub, when employing Docker as the containerization solution. Second, the computational workflow's input/output interfaces and the orchestration of its command-line tools are described using a formal specification such as the Common Workflow Language (CWL) (Parasyris et al., 2024).

This approach enhances usability and facilitates rapid adaptation to dynamic conditions, enabling the generation of forecasts that are timely and precise. For example, this methodology supports the generation of forecasts under adverse meteorological conditions within the port environment, allowing for more accurate predictions to be conducted closer to the onset of an impending storm. This timing improves the reliability of the forecasts by leveraging shorter lead times, which are typically associated with higher predictive accuracy (Parasyris et al., 2022; Swatridge et al., 2024; Valiente et al., 2023).

Furthermore, cataloguing these application packages enhances their discoverability and provides metadata that comprehensively describe the workflow, including its inputs, outputs, contributors, and other relevant details. This enables clear differentiation between versions of the application package. From a security perspective, access to these packages can be restricted, ensuring the safeguarding of intellectual property and enabling potential commercialization. As an example, the SWAN application package is catalogued and openly available at https://github.com/ILIAD-ocean-twin/application_package/tree/main/SWAN_Heraklion (last accessed 04/2025).

2.3 Overtopping Discharges

The forecasted waves are used for monitoring extreme conditions and safety of the port for the visitors, based on wave overtopping estimations (Van der Meer et al. 2018). The pier region is divided in two parts, the left (yellow outline in) and the right (blue outline in Fig. 2), based on the different armoring of the breakwater. By making this distinction, we adapt the equations used for each case. More specifically, on the left case study, the addition of accropodes to the armoring makes the case similar to case study 8 of the EurOtop manual (Van der Meer et al. 2018) with concrete armor breakwater, while on the right case study, the situation resembles a composite vertical wall without a foreshore. The equations that can be used for the calculation of the discharge q in both cases are shown in Table 1.

Table 1. Equations for overtopping calculations at each case [10]. In all equations coefficients γ_β, γ_f, = 1 and the freeboard height is R_c=4 m

Case Study	Overtopping Equations
Left	$\frac{q}{\sqrt{gH_{mo}^3}} = 0.1035 exp\left(-\left(1.35\frac{R_c}{H_{m0}\cdot\gamma_f\cdot\gamma_\beta}\right)^{1.3}\right)$ *suitable for steep slopes 1:2 to 1:4/3*
Right	$\frac{q}{\sqrt{gH_{mo}^3}} = 0.047 exp\left[-\left(2.35\frac{R_c}{H_{m0}}\right)^{1.3}\right]$

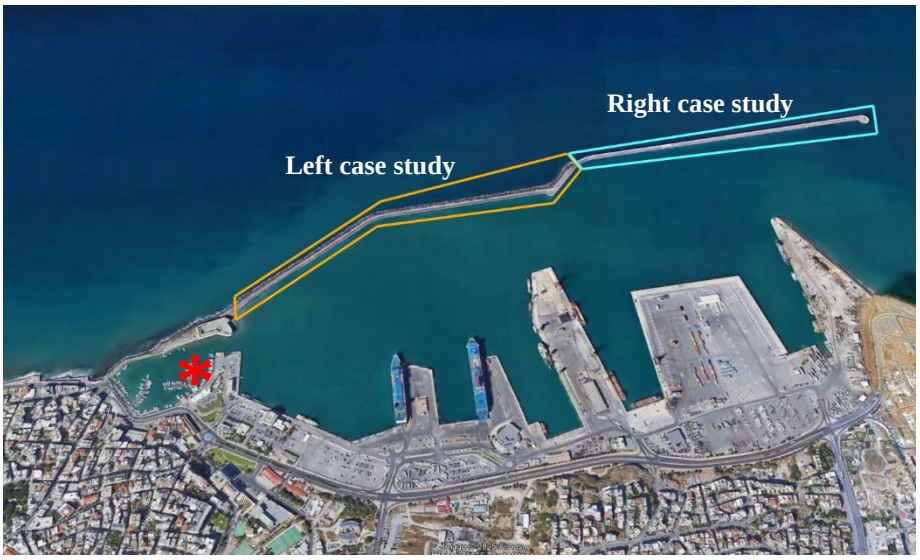

Fig. 2. Map of test case in northwestern coastal area of Heraklion, split in 2 case studies, denoted by different colors and red star indicating the location of the meteorological station within the port. Aerial view of Heraklion coast from Google Earth, captured on 10/3/2022 (© Google Earth, 2023, LLC)

3 Results

In this section, the model's validation and wave analysis are presented. The available SWAN50 hourly results for the datetime range of 23/10/2024-9/1/2025, are used for the model validation and subsequent analysis.

3.1 Model Validation

In the absence of direct in-situ or satellite measurements for the region, the model results regarding the first forecast day, are validated using SWH and peak period (Tp, in s) estimates derived from the JONSWAP formula applied to wind data from the nearest meteorological station, located at the port area (Fig 2). Furthermore, validation is performed against the CMEMS 4 km wave forecast and analysis product, as it is considered the closest representation of ground truth (Fig 3). The forecasted values of the SWAN50 SWH and Tp are extracted as the mean values of the 4x4 grid box centered at the locations annotated in Fig 1b, as SWAN-N, SWAN-W, SWAN-E and SWAN-P. For the CMEMS product the closest grid point to the domain coordinates is selected. For the quantification of the results, a series of statistical parameters are calculated at each aforementioned location in and nearby the port area, namely Pearson's r, Root Mean Squared Error (RMSE), Mean Bias Error (MBE), and Mean Absolute Error (MAE) (Table 2, 3). A 3-hour moving average has been applied to the JONSWAP

SWH estimation to mitigate the discretization effects inherent in the original formulation, which classifies values into specific bins. This adjustment ensures a more continuous representation of wave height, facilitating a more consistent comparison with model outputs that exhibit smoother variations in alignment with the underlying physical processes.

In Fig 3a, the SWH values of the SWAN-N, SWAN-W, SWAN-E are in close proximity to the CMEMS, with r=0.95 and low errors with RMSE=0.22 up to 0.24 m, MBE=0.08 up to 0.15 m and MAE=0.16 up to 0.19 m (Table 2). The SWAN-P expresses lower values, r=0.93 and higher errors with RMSE=0.82 m, MBE=0.67 m and MAE=0.67 m (Table 2), as expected, but with the same fluctuations to the other locations. Additionally, some parts of the SWAN timeseries are close to the JONSWAP approximation results, but for the most part the results don't coincide. This can be attributed to the approximation nature of the JONSWAP formula, which can only give a rough estimate based on wind data (Hasselmann et al., 1973). Although the JONSWAP empirical model is an approximation derived under deep-water, fetch-limited conditions, and its direct applicability to semi-enclosed environments such as harbors is limited, it remains a valuable qualitative reference in the absence of in-situ wave observations. The statistical values reveal r=0.40 up to 0.45, and higher errors in relation to the CMEMS comparison, with RMSE=0.93 up to 1.18 m, MBE=0.04 up to 0.68 m, MAE=0.67 up to 0.75 m.

The Tp time series, displayed in Fig 3b, reveal similar results. The SWAN50 results, at all locations, are in good proximity to the CMEMS values with r=0.76 at the SWAN-N, E, W and low error values with RMSE=1.13 up to 1.4 s, MBE=-0.28 to -0.29 s and MAE=0.61 to 0.62 s (Table 2). At the SWAN-P location, r=0.74 and errors with RMSE=1.24 m, MBE=-0.54 m and MAE=0.74 m (Table 2). The higher errors in the SWAN-P are attributed to the CMEMS grid resolution, which cannot adequately capture the fine resolution of the port inside the pier (Fig. 1b) which is well represented by the bathymetry dataset of the presented SWAN50 model. The JONSWAP results again have low overlap with low r=0.09 up to 0.15, RMSE=4.08 up to 4.28 s, MBE=-2.59 to -2.84 s, and MAE=3.30 up to 3.47 s.

Table 2. Statistical parameters used for the validation of the 1st day of SWH forecast from SWAN50 model against the JONSWAP (JS) estimated SWH from the meteorological station's data (number of observations, N=477) and the SWH from CMEMS (N=1896). R is the Pearson's correlation coefficient, RMSE the Root Mean Squared Error (m), MBE the Mean Bias Error (m), and MAE the Mean Absolute Error (m). N, E, W, P correspond to the mean SWH of a 4x4 grid box centered at the respected annotated locations in Fig. 1

	r		RMSE		MBE		MAE	
	JS	CMEMS	JS	CMEMS	JS	CMEMS	JS	CMEMS
SWAN-N	0.45	0.94	0.93	0.22	0.04	0.08	0.68	0.16
SWAN-E	0.44	0.94	0.93	0.24	0.09	0.12	0.67	0.17
SWAN-W	0.45	0.94	0.93	0.24	0.11	0.15	0.67	0.19
SWAN-P	0.39	0.92	1.18	0.82	0.68	0.67	0.75	0.67

Table 3. Same as Table 2, for the Tp. RMSE, MBE and MAE in s

	r		RMSE		MBE		MAE	
	JS	CMEMS	JS	CMEMS	JS	CMEMS	JS	CMEMS
SWAN-N	0.14	0.76	4.10	1.13	-2.61	-0.29	3.31	0.61
SWAN-E	0.13	0.76	4.11	1.14	-2.62	-0.29	3.32	0.61
SWAN-W	0.15	0.76	4.08	1.4	-2.59	-0.28	3.30	0.62
SWAN-P	0.09	0.74	4.28	1.24	-2.84	-0.54	3.47	0.74

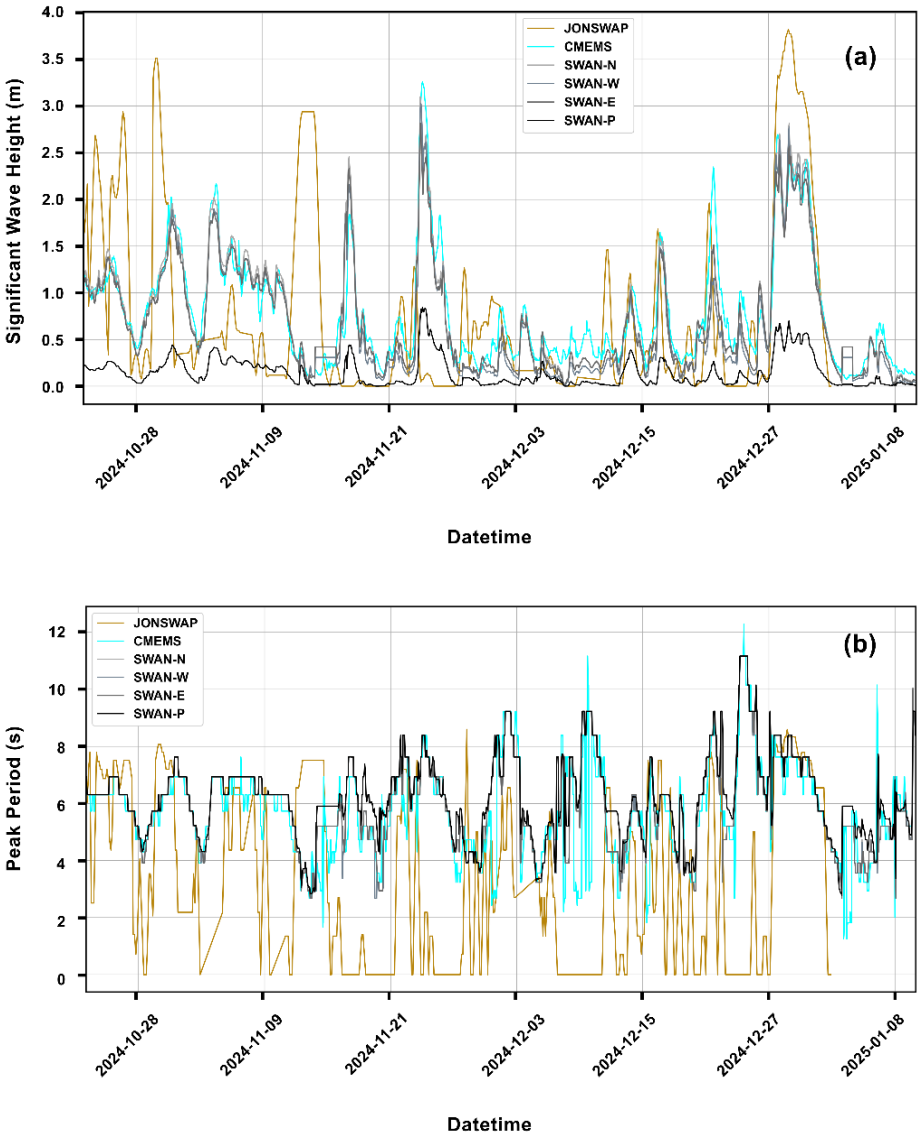

Fig. 3. (a) Time Series of the Significant Wave Height (SWH) as estimated from the meteorological station's data using the JONSWAP formula (JONSWAP), from the CMEMS platform (CMEMS), and calculated as the mean value of a 4x4 grid box, centered at the corresponding locations on the north, west, and east outside of the pier (SWAN-N, SWAN-W, SWAN-E) and on the port (SWAN-P) (Fig. 1). (b) The same for peak Period (Tp)

3.2 Forecasting Stability

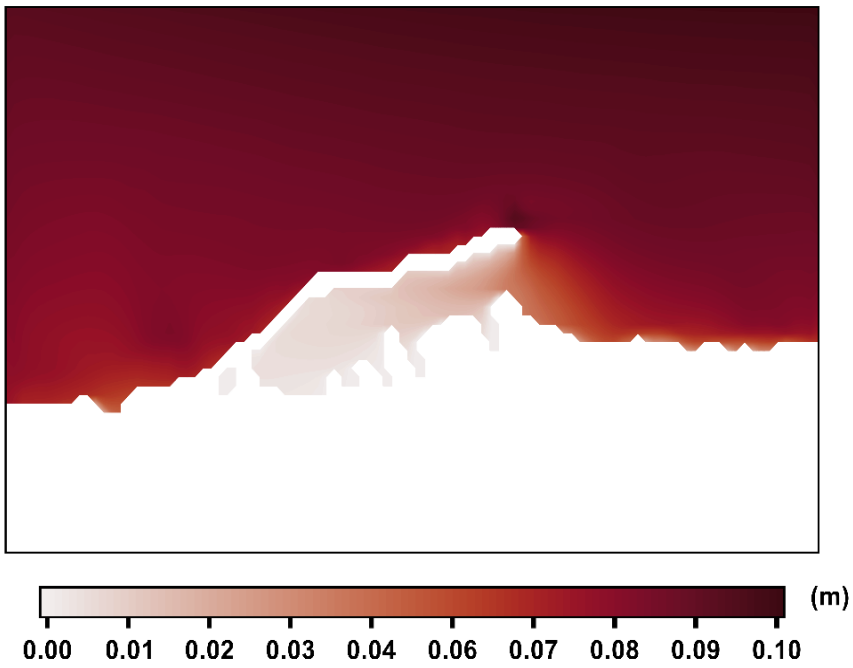

Fig. 4. Absolute mean bias error between the overlapping forecasts of first and second days of SWAN50 outputs, averaged over all the time steps at each grid point

To assess the stability of our model and investigate the spatial variability between day-1 and day-2 forecasts, the National Meteorological Center (NMC) method is applied. NMC, originally introduced by Parrish and Derber (Parrish & Derber, 1992), is widely utilized for evaluating model errors in regional studies (Lam et al., 2021; Parrish & Derber, 1992). It assumes that model errors can be effectively characterized using statistical data derived from averaged forecast differences, typically calculated over a series of forecasts with different lead times, valid at the same time. In this study, the Mean Absolute Bias Error (MABE) as is calculated at each grid point:

$$MABE = \Sigma|SWH_{day1} - SWH_{day2}|/\,N, \quad (1)$$

where SWH_{day1} and SWH_{day2} are the models' overlapping forecasts, resulting from first and second day forecasts, and N is the number of measurements, which in this case is 1896 the number of timesteps over which the mean is calculated.

Investigating Fig. 4, the port region presents lower MABE values (<0.02 m), while for the rest of the domain MABE is higher and up to 0.10 m. This is expected as the port has a lower magnitude of mean SWH to the rest of the domain. Specifically, the mean SWH at the location inside the port (point P Fig. 1) is 0.14 m (forecast day-1) and

0.12m (forecast day 2) whereas outside the port in the other 3 locations selected (points W, N, E Fig. 1), we calculate a range of 0.66-0.74 m (forecast day-1) and 0.61-0.68 m (forecast day-2).

3.3 Wave analysis

Fig.5 illustrates the mean SWH field of the region, with waves following a S, S-SE direction outside the piers, and going to the SW inside the piers. The SWH outside the piers are larger, going up to 0.8 m on average, while inside the piers the value drops at 0.10 m.

Analyzing the wave field further, the prevailing wave direction for the SWAN50 outside the pier is towards the S-SE (Fig. 6a-c), at 38.12% at SWAN-N (Fig.6a), 41.9% for SWAN-E (Fig.6b) and 37.53% at SWAN-W (Fig.6c). The next major direction is the SE at 37.11% at SWAN-N, 36.90% at SWAN-E and 33.75% at SWAN-W, followed by the S, S-SW which combined cover approximately 10% of the remaining frequencies at these locations. Regarding the SWH values, approximately 50% are in the range of 0.0-0.5 m, 20% at 0.5-1.0 m, 20% at 1.0-1.5 m, 5% at 1.5-2.0 m, while the rest 5% is above 2.0 m.

Results differ at the SWAN-P location where the prevailing wave direction at 95.18% is towards the W, with the remaining 4.82% covering the W-NW and W-SW directions (Fig.6d). Approximately 50% of SWH values are in the range of 0.0-0.1 m, 32% at 0.1-0.3 m, 10% at 0.3-0.5 m, while the rest is above 0.5 m.

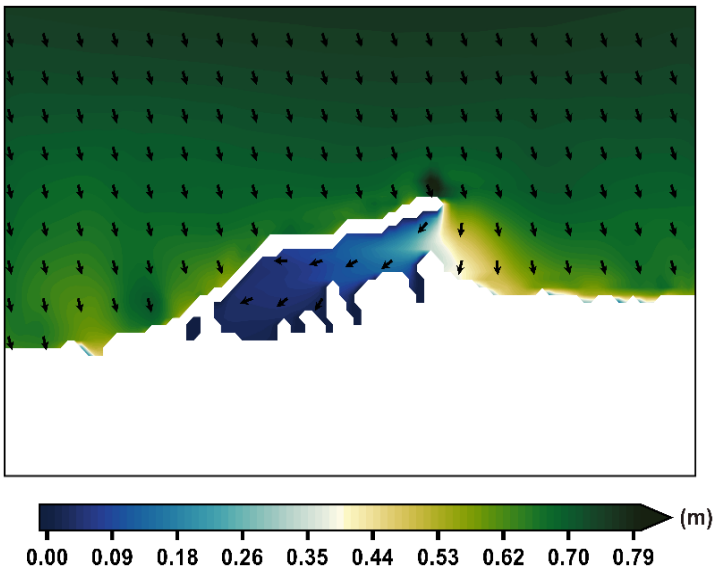

Fig. 5. The SWAN50 SWH field, averaged over the results period (23/10/2024-9/1/2025), with overlapping wave direction arrows

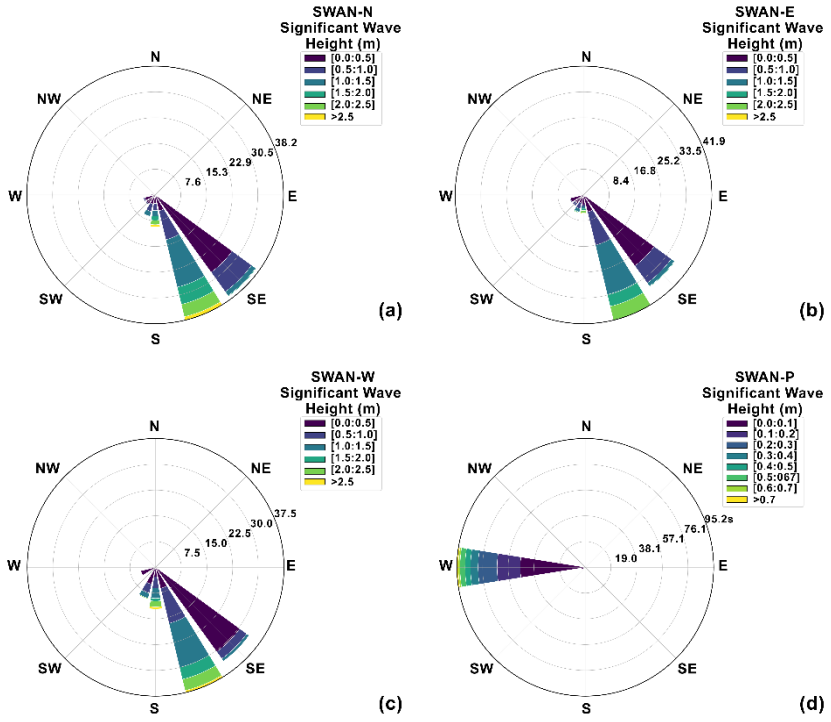

Fig. 6. Waveroses (wave direction to; normalized) for the (a) SWAN-N, (b) SWAN-E, (c) SWAN-W and (d) SWAN-P locations (Fig. 1.)

The associated wind speed and direction is also examined in Fig. 7. Dominant wind directions appear to be from S-SW to W-SW, and from W-NW and NW. Stronger winds (>14 m/s) are rare but present, mostly from W-NW to N-NW. Specifically, 16.14% of wind is coming from the SW, 13.63% from the W-NW, 11.5% from the S-SW and 10.90% from the NW. Additionally, 45% of wind speed values are between 0-6 ms^{-1}, 33% are between 6-10 ms^{-1}, 18% are between 10-14 ms^{-1}, and the remaining is over 14 ms^{-1}.

3.4 Extreme Conditions

The main purpose of the SWAN50 is accurately forecasting the wave field, providing a realistic representation of extreme wave conditions required for harbor safety applications. The top 6-7% of the available SWAN50's SWH corresponds to values greater than 2 m outside the pier at the SWAN-N, E, W locations, and greater than 0.5 m at the SWAN-P location.

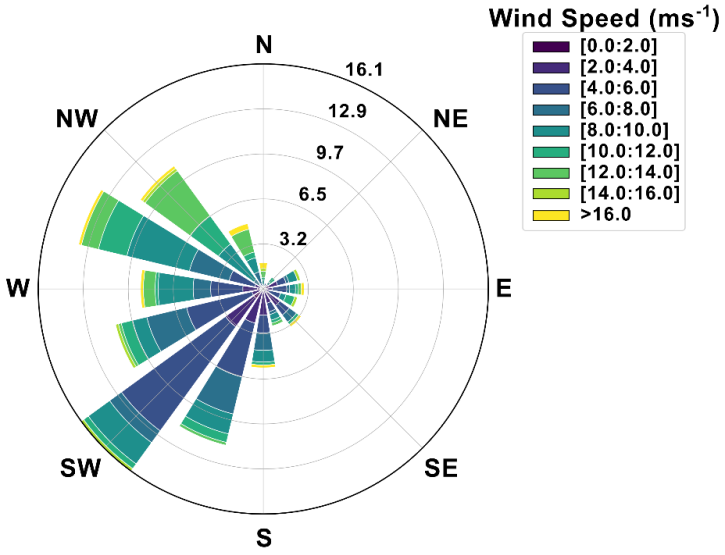

Fig. 7. Windrose (wind direction from; normalized) of the station's time series, covering the SWAN50 results' datetime period

In SWAN-N, E, W location's 97% waves of SWH>2 m are directed towards the S and S-SE, while the remaining 3% have a direction towards S-SW. Inside the port, in SWAN-P, all the waves with SWH>0.5 m, are towards the W.

In Fig. 8, the wind speed and direction associated with SWH>2 m (in locations SWAN-N, E, W) during the time of the model's results (October-January) are presented. Approximately 71% of the wind is coming from the W-NW-N. The greater wind speeds (>10 ms-1) also originate from these directions.

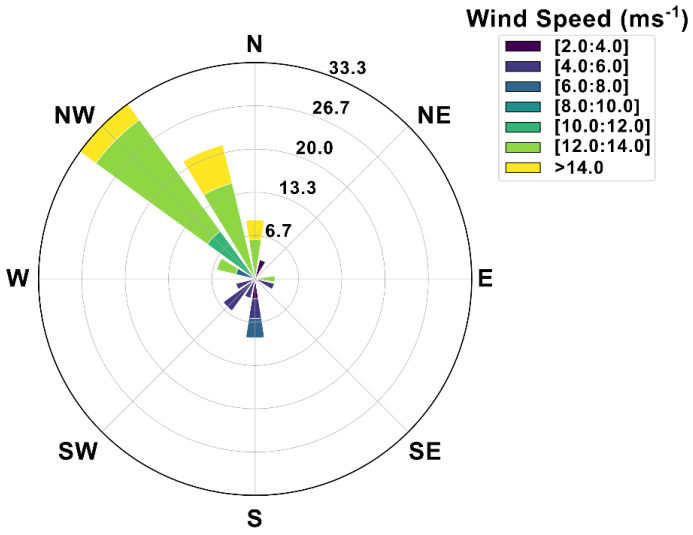

Fig. 8. Windrose (wind direction from; normalized) corresponding to the winds associated with the most extreme waves detected in the SWAN50 time series after applying a SWH threshold of 2 m (corresponding to the top 5% of SWH)

Fig. 9 presents the SWAN50 results for the datetime of the highest mean field SWH value of the dataset (2.73 m), which corresponds to 24/11/2024 00:00. The overall wave pattern is similar to Fig. 5, with the waves outside the port traveling towards the S, while inside the piers they follow the W direction. Additionally, the SWH is much lower inside the piers with values at 0.40 m on average, while in relation to the outside SWH reaches up to 3.26 m.

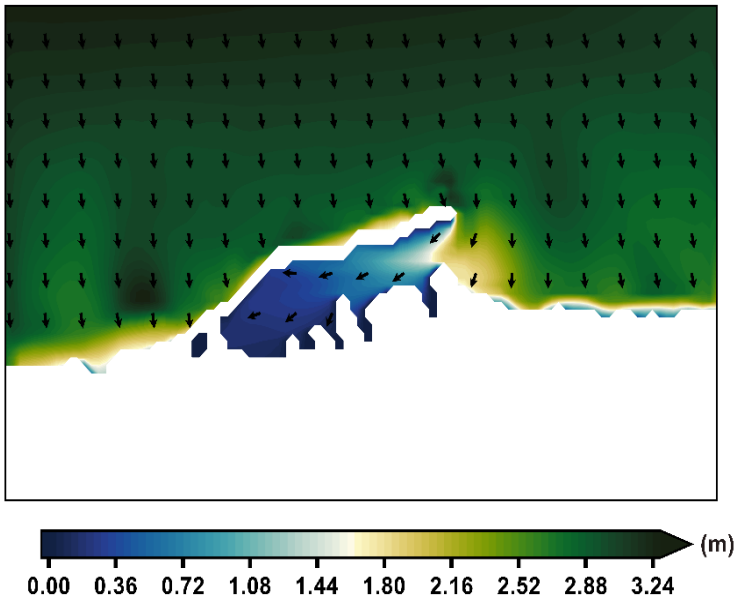

Fig. 9. The SWH field, with overlapping wave direction arrows, on the 24th of November 2024, corresponds to the highest SWAN50's SWH value of the time series dataset

3.5 Wave Overtopping

Fig. 10 configurations. Fig. 10a represents a concrete-armored breakwater with accropodes, while Fig. 10b corresponds to a composite wall with no foreshore. The results reveal a clear distinction in overtopping severity between the two cases.

In Fig. 10a, the overtopping discharge remains below 2.5 l/s/m, which, according to safety thresholds (Van der Meer et al. 2018), falls mainly within the moderate to significant overtopping range ($0.1 < q < 10$ l/s/m). While some wave overtopping occurs, it is generally not hazardous for pedestrians or vehicles under normal conditions. However, during strong wave events, localized water accumulation and splashing on the breakwater crest could still pose a slipping risk for pedestrians or cause minor operational disruptions.

In contrast, Fig. 10b shows significantly higher overtopping discharges, with values exceeding 5 l/s/m in multiple instances with some peaks approaching the severe over-

topping threshold (q > 10 l/s/m). In such cases, harbor safety is significantly compromised, as water volumes reaching the crest may become dangerous for people walking on or near the breakwater. High overtopping events at this level can cause sudden waves washing over the structure, knocking down pedestrians, flooding access roads, and even damaging vehicles. The lack of a foreshore in this case results in waves directly impacting the structure, allowing uncontrolled water surges that can make the breakwater unsafe for public access.

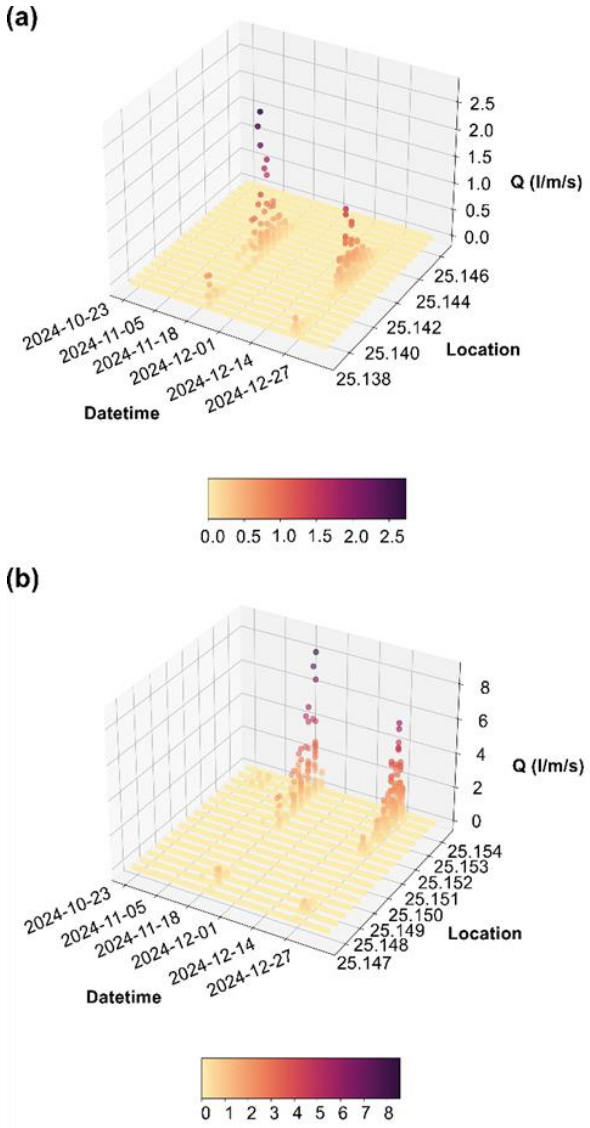

Fig. 10. The wave overtopping, Q (l/m/s), is estimated in the outside region of the pier. (a) Q time series estimated at the left side of the pier, and (b) at the right side of the pier at each grid point (Location, in ^{o}E)

4 Discussion

This study presents a high-resolution wave forecasting framework for the Heraklion Port region, providing a 2-day hourly forecast of wave-related parameters at 50 m horizontal resolution. The fine spatial resolution and detailed representation of the region's bathymetry and coastal structures significantly enhance the accuracy of the results, making them suitable for harbor safety applications. The complex orography of Crete plays a crucial role in shaping local wind patterns, which in turn influence wave generation and propagation (ref). Consequently, the resolution of both the wind forcing and wave modeling is critical in minimizing forecast errors (De Girolamo et al., 2017).

The validation of the modeled significant wave height (SWH) demonstrates strong agreement with the CMEMS product (Fig. 3, Tables 1,2). Outside the port piers, the SWAN50 model closely follows the CMEMS dataset, indicating its ability to capture regional wave dynamics effectively (Fig. 5). Inside the port, SWH values are significantly lower, as expected, due to the presence of the piers, which act as a protective barrier against incoming waves (Fig 5). The increased accuracy of SWAN50 is attributed to its fine grid resolution (50 m), which is 80 times higher than the CMEMS product, and the inclusion of a detailed bathymetric representation of port structures. In contrast, the CMEMS bathymetry lacks these features, leading to less realistic nearshore wave conditions. A similar validation was conducted for peak wave period (Tp), further supporting the model's reliability.

The findings of this study align with previous research on wave dynamics in the Aegean Sea, particularly concerning wave heights, wind speeds, and prevailing wind patterns. Soukissian et al. (2008) conducted a comprehensive analysis of wind and wave data in the Aegean Sea, identifying a predominance of northerly winds, commonly referred to as the Etesian winds, especially during the summer months. These persistent northerly winds significantly influence wave conditions, leading to higher wave heights and energy fluxes directed towards the southern parts of the Aegean. Similarly, Zacharioudaki et al. 2015 utilized high-resolution wave modeling to study the impact of wind patterns on wave characteristics in the region, confirming that the dominant wave directions are closely linked to the prevailing northerly winds. Poulos et al. (1997) also highlighted the influence of these seasonal wind patterns on the hydrodynamics of the Aegean Sea, noting occasional southerly winds that can alter local wave conditions.

Analysis of the modeled period (23 October 2024 – 9 January 2025) indicates that waves primarily propagate towards the SE and E, driven by W and NW winds (Fig. 6). Outside the port, wave directions predominantly range from S-SE to SE (Fig. 6a-c), while inside the port, waves are redirected westward due to the influence of port structures (Fig. 6d). SWH values outside the piers reach up to 3.2 m, with most waves being below 2 m. Waves exceeding 2 m primarily propagate towards the SE. Inside the port, SWH values range from 0.0 to 0.5 m, occasionally reaching 0.8 m, and fluctuate according to the external wave field.

Wind conditions, as recorded by the meteorological station, further validate the modeled wave dynamics (Fig. 8). The wind field exhibits high temporal and directional variability, with the strongest winds originating from W-NW to N-NW, and secondary contributions from S-SW to W-SW. The relationship between wind forcing and wave

conditions indicates that waves exceeding 2 m are primarily generated by NW to N winds exceeding 12 m/s, propagating towards the SE and S.

Given that Heraklion Port is exposed to the SE and E, wave activity in the port is predominantly influenced by W and NW winds. A strong correlation (r = 0.93) is observed between SWH inside and outside the port, highlighting the dependence of port wave conditions on external wave forcing. A least-squares regression between the SWH at SWAN-P (inside the port) and SWAN-N (outside the port) yields the relationship:

$$SWH_{SWAN\text{-}P} = 0.2414 * SWH_{SWAN\text{-}N} - 0.0366\ m.$$

Understanding these patterns is crucial for navigational safety, mooring operations, and port infrastructure planning (Dahle & Myrhaug, 1995; De Girolamo et al., 2017; Gomes et al., 2022; Niclasen et al., 2010; Pinheiro et al., 2022; Samaras et al., 2016). The findings of this study emphasize the importance of high-resolution wave modeling in improving local-scale wave forecasts, thereby enhancing maritime safety and port management strategies. The results underscore the importance of precise wave modeling in predicting harbor resonance phenomena and informing the design of effective wave mitigation strategies. By integrating such high-resolution models into port management practices, stakeholders can better anticipate and respond to adverse wave conditions, improving maritime safety and operational efficiency.

Although SWAN does not resolve phase-coherent processes such as diffraction and reflection in detail, especially in complex harbor geometries, it remains suitable for simulating regional wave fields and providing input for nested, high-resolution models. The current study prioritizes broader wave conditions over detailed near-boundary interference patterns. Several studies have demonstrated the value of using wave agitation models to optimize port operations (Chondros et al., 2024; Diaz-Hernandez et al., 2021; Tsoukala et al.,2016). Nonetheless, future applications may benefit from coupling with phase-resolving models for higher fidelity.

From a harbor management perspective, the results suggest that breakwaters with wave-dissipating structures like accropodes (Fig. 10a) provide a safer environment for pedestrian walkways, port workers, and vehicles, as they limit hazardous overtopping. In contrast, breakwaters without foreshores or energy-dissipating elements (Fig. 10b) are much more prone to extreme overtopping events that require access restrictions during high wave conditions.

For operational safety, Fig. 10b suggests the need for protective measures, such as railings, warning systems, restricted pedestrian access during extreme wave events, or modifications to reduce overtopping, such as crest height adjustments or additional energy dissipation features. Given the high frequency of overtopping events in this case, harbor authorities should assess whether the structure remains safe for regular use or requires interventions to minimize risk to both people and vehicles.

5 Conclusion

The findings of this study align with previous research on wave dynamics in the Aegean Sea, particularly concerning wave heights, wind speeds, and prevailing wind patterns.

The study demonstrates that high-resolution wave modeling can improve local-scale wave forecasts, reducing uncertainties in port wave conditions and supporting decision-making for harbor safety. The integration of numerical wave models such as SWAN50 with operational forecasting systems provides a powerful tool for predicting hazardous conditions, allowing for timely interventions to protect maritime operations, infrastructure, and personnel.

Furthermore, this study highlights the importance of considering overtopping hazards in harbor safety assessments. The results indicate that breakwater design plays a critical role in mitigating overtopping risks, with structures incorporating wave-dissipating elements significantly reducing hazardous conditions. In contrast, structures without foreshore protection experience frequent overtopping events, which may necessitate access restrictions, additional protective measures, or design modifications.

As climate change continues to intensify extreme wave events, the role of real-time operational forecasting and high-resolution modeling will become increasingly critical in coastal infrastructure planning and risk mitigation. Future work should incorporate long-term climate projections and sea-level rise scenarios to assess their impact on wave overtopping and harbor safety. By continuously improving forecasting models and integrating them into coastal management strategies, it is possible to enhance the resilience of port infrastructure and ensure safe and sustainable maritime operations.

Acknowledgments

This project has received funding from the European Commission's Horizon 2020 Research and Innovation programme under grant agreements no. 101037643.

References

1. Becker, A. H., Acciaro, M., Asariotis, R., Cabrera, E., Cretegny, L., Crist, P., Esteban, M., Mather, A., Messner, S., Naruse, S., Ng, A. K. Y., Rahmstorf, S., Savonis, M., Song, D. W., Stenek, V., & Velegrakis, A. F. (2013). A note on climate change adaptation for seaports: A challenge for global ports, a challenge for global society. Climatic Change, 120(4), 683–695. https://doi.org/10.1007/S10584-013-0843-Z/TABLES/1
2. Bidlot, J.-R. C. M. W. F. (n.d.). Present Status of Wave Forecasting at E. Retrieved February 12, 2025, from http://www.ecmwf.int/research/ifsdocs/
3. Booij, N., Ris, R. C., & Holthuijsen, L. H. (1999). A third-generation wave model for coastal regions: 1. Model description and validation. Journal of Geophysical Research: Oceans, 104(C4), 7649–7666. https://doi.org/10.1029/98JC02622
4. Breivik, Ø., Aarnes, O. J., Bidlot, J. R., Carrasco, A., & Saetra, Ø. (2013). Wave Extremes in the Northeast Atlantic from Ensemble Forecasts. Journal of Climate, 26(19), 7525–7540. https://doi.org/10.1175/JCLI-D-12-00738.1

5. Breivik, Ø., Mogensen, K., Bidlot, J. R., Balmaseda, M. A., & Janssen, P. A. E. M. (2015). Surface wave effects in the NEMO ocean model: Forced and coupled experiments. Journal of Geophysical Research: Oceans, 120(4), 2973–2992. https://doi.org/10.1002/2014JC010565
6. Cavaleri, L., & Rizzoli, P. M. (1981). Wind wave prediction in shallow water: Theory and applications. Journal of Geophysical Research: Oceans, 86(C11), 10961–10973. https://doi.org/10.1029/JC086IC11P10961
7. Chatzinikolaou, E., & Arvanitidis, C. (2016). Status, values and present threats in Heraklion harbour (Crete, Greece). Regional Studies in Marine Science, 8, 252–258. https://doi.org/10.1016/J.RSMA.2016.01.010
8. Chlomoudis, C., Kostagiolas, P., Pallis, P., & Platias, C. (2024). Quality, Safety, and Security Systems in the Greek Port Industry: Over Twenty Years of Research, Empirical Evidence, and Future Perspectives. Logistics 2024, Vol. 8, Page 98, 8(4), 98. https://doi.org/10.3390/LOGISTICS8040098
9. Chondros, M. K., Metallinos, A. S., & Papadimitriou, A. G. (2024). Enhanced Mild-Slope Wave Model with Parallel Implementation and Artificial Neural Network Support for Simulation of Wave Disturbance and Resonance in Ports. Journal of Marine Science and Engineering 2024, Vol. 12, Page 281, 12(2), 281. https://doi.org/10.3390/JMSE12020281
10. Dahle, E. A., & Myrhaug, D. (1995). Risk Analysis Applied to Capsize of Fishing Vessels. Marine Technology and SNAME News, 32(04), 245–247. https://doi.org/10.5957/MT1.1995.32.4.245
11. De Girolamo, P., Di Risio, M., Beltrami, G. M., Bellotti, G., & Pasquali, D. (2017). The use of wave forecasts for maritime activities safety assessment. Applied Ocean Research, 62, 18–26. https://doi.org/10.1016/j.apor.2016.11.006
12. Diaz-Hernandez, G., Rodríguez Fernández, B., Romano-Moreno, E., & L. Lara, J. (2021). An improved model for fast and reliable harbour wave agitation assessment. Coastal Engineering, 170, 104011. https://doi.org/10.1016/J.COASTALENG.2021.104011
13. EMODnet Bathymetry Consortium. (2022). EMODnet Digital Bathymetry (DTM 2022). https://doi.org/doi:10.12770/ff3aff8a-cff1-44a3-a2c8-1910bf109f85
14. Gomes, A. H., Pinheiro, L. V., Fortes, C. J. E. M., & Santos, J. A. (2022). Applying the SAFEPORT system in a storm situation. Trends in Maritime Technology and Engineering Volume 2, 205–212. https://doi.org/10.1201/9781003320289-22
15. Hasselmann, K., Barnett, T. P., Bouws, E., Carlson, H., Cartwright, D. E., Enke, K., Ewing, J. A., Gienapp, A., Hasselmann, D. E., Kruseman, P., Meerburg, A., Müller, P., Olbers, D. J., Richter, K., Sell, W., & Walden, H. (1973). Measurements of wind-wave growth and swell decay during the joint North Sea wave project (JONSWAP). Ergänzungsheft Zur Deutschen Hydrographischen Zeitschrift, Reihe A, Nr. 12. https://www.researchgate.net/publication/256197895
16. Hong, Z., et al. (2013). The Competitiveness of Global Port-Cities: The Case of Shanghai, China: Vol. 2013/23 (OECD Regional Development Working Papers). https://doi.org/10.1787/5k3wd3bnz7tb-en
17. Korres, G., Oikonomou, C., Denaxa, D., & Sotiropoulou, M. (2023). Mediterranean Sea Waves Analysis and Forecast (Copernicus Marine Service MED-Waves, MEDWAM4 system) (Version 1) [Data set]. Copernicus Marine Service (CMS).
18. Lam, M., Fung, J. C., Rancic, M., & Lupo, A. R. (2021). Model Sensitivity Evaluation for 3DVAR Data Assimilation Applied on WRF with a Nested Domain Configuration.

Atmosphere 2021, Vol. 12, Page 682, 12(6), 682. https://doi.org/10.3390/ATMOS12060682

19. Makris, C., Papadimitriou, A., Baltikas, V., Spiliopoulos, G., Kontos, Y., Metallinos, A., Androulidakis, Y., Chondros, M., Klonaris, G., Malliouri, D., Nagkoulis, N., Zissis, D., Tsoukala, V., Karambas, T., & Memos, C. (2024). Validation and Application of the Accu-Waves Operational Platform for Wave Forecasts at Ports. Journal of Marine Science and Engineering, 12(2), 220. https://doi.org/10.3390/JMSE12020220/S1
20. Niclasen, B. A., Simonsen, K., & Magnusson, A. K. (2010). Wave forecasts and small-vessel safety: A review of operational warning parameters. Marine Structures, 23(1), 1–21. https://doi.org/10.1016/J.MARSTRUC.2010.02.001
21. Papadopoulos, G. A., & Dermentzopoulos, T. (1998). A Tsunami Risk Management Pilot Study in Heraklion, Crete. Natural Hazards, 18(2), 91–118. https://doi.org/10.1023/A:1008070306156/METRICS
22. Parasyris, A., Alexandrakis, G., Kozyrakis, G. V., Spanoudaki, K., & Kampanis, N. A. (2022). Predicting Meteorological Variables on Local Level with SARIMA, LSTM and Hybrid Techniques. Atmosphere 2022, Vol. 13, Page 878, 13(6), 878. https://doi.org/10.3390/ATMOS13060878
23. Parasyris, A., Metheniti, V., Alexandrakis, G., Kozyrakis, G. V., & Kampanis, N. A. (2024). Data Assimilated Atmospheric Forecasts for Digital Twin of the Ocean Applications: A Case Study in the South Aegean, Greece. Algorithms, 17(12), 586. https://doi.org/10.3390/a17120586
24. Parrish, D. F., & Derber, J. C. (1992). The National Meteorological Center's Spectral Statistical-Interpolation Analysis System. Monthly Weather Review, 120(8), 1747–1763. https://doi.org/10.1175/1520-0493(1992)120<1747:TNMCSS>2.0.CO;2
25. Pinheiro, L., Gomes, A., Fortes, C., & Santos, J. A. (2022). Safety System for Ships in Harbours. In Progress in Marine Science and Technology (Vol. 6, pp. 580–587). E. Rizzuto and V. Ruggiero. https://doi.org/10.3233/PMST220069
26. Poulos, S. E., Drakopoulos, P. G., & Collins, M. B. (1997). Seasonal variability in sea surface oceanographic conditions in the Aegean Sea (Eastern Mediterranean): an overview. Journal of Marine Systems, 13(1–4), 225–244. https://doi.org/10.1016/S0924-7963(96)00113-3
27. Samaras, A. G., Gaeta, M. G., Miquel, A. M., & Archetti, R. (2016). High-resolution wave and hydrodynamics modelling in coastal areas: Operational applications for coastal planning, decision support and assessment. Natural Hazards and Earth System Sciences, 16(6), 1499–1518. https://doi.org/10.5194/NHESS-16-1499-2016
28. Sierra, J. P., Casas-Prat, M., Virgili, M., Mösso, C., & Sánchez-Arcilla, A. (2015). Impacts on wave-driven harbour agitation due to climate change in Catalan ports. Natural Hazards and Earth System Sciences, 15(8), 1695–1709. https://doi.org/10.5194/NHESS-15-1695-2015
29. Soukissian, T., Prospathopoulos, A., Hatzinaki, M., & Kabouridou, M. (2008). Assessment of the Wind and Wave Climate of the Hellenic Seas Using 10-Year Hindcast Results. The Open Ocean Engineering Journal, 1(1), 1–12. https://doi.org/10.2174/1874835X00801010001
30. Swatridge, L. L., Mulligan, R. P., Boegman, L., & Shan, S. (2024). Development and performance of a high-resolution surface wave and storm surge forecast model: Application to a large lake. Geoscientific Model Development, 17(21), 7751–7766. https://doi.org/10.5194/GMD-17-7751-2024
31. Tsoukala, V. K., Chondros, M., Kapelonis, Z. G., Martzikos, N., Lykou, A., Belibassakis, K., & Makropoulos, C. (2016). An integrated wave modelling framework for extreme

and rare events for climate change in coastal areas – the case of Rethymno, Crete. Oceanologia, 58(2), 71–89. https://doi.org/10.1016/J.OCEANO.2016.01.002

32. Valiente, N. G., Saulter, A., Gomez, B., Bunney, C., Li, J. G., Palmer, T., & Pequignet, C. (2023). The Met Office operational wave forecasting system: the evolution of the regional and global models. Geoscientific Model Development, 16(9), 2515–2538. https://doi.org/10.5194/GMD-16-2515-2023
33. Van der Meer, J. W., Allsop, N. W. H., Bruce, T., De Rouck, J., Kortenhaus, A., Pullen, T., Schüttrumpf, H., Troch, P., & Zanuttigh, B. (2018). EurOtop. Manual on wave overtopping of sea defences and related structures. www.overtopping-manual.com
34. Vousdoukas, M. I., Mentaschi, L., Voukouvalas, E., Bianchi, A., Dottori, F., & Feyen, L. (2018). Climatic and socioeconomic controls of future coastal flood risk in Europe. NATURE CLIMATE CHANGE, 8(9),776–780. https://doi.org/10.1038/S41558-018-0260-4
35. Zacharioudaki, A., Korres, G., & Perivoliotis, L. (2015). Wave climate of the Hellenic Seas obtained from a wave hindcast for the period 1960–2001. Ocean Dynamics, 65(6), 795–816. https://doi.org/10.1007/S10236-015-0840-Z/FIGURES/23